

BLACK HOLE—BLACK HOLE TOTAL MERGER MASS AND THE ORIGIN OF LIGO/VIRGO SOURCES

KRZYSZTOF BELCZYNSKI¹, ZOHEYR DOCTOR², MICHAEL ZEVIN^{3,4}, ALEKSANDRA OLEJAK¹, SAMBARAN BANERJEE^{4,5},
DEBATRI CHATTOPADHYAY⁶

¹ Nicolaus Copernicus Astronomical Center, Polish Academy of Sciences, Bartycka 18, 00-716 Warsaw, Poland
(chrisbelczynski@gmail.com, aleksandra.olejak@wp.pl)

² Center for Interdisciplinary Exploration and Research in Astrophysics (CIERA) and Department of Physics & Astronomy,
Northwestern University, 1800 Sherman Ave, Evanston, IL 60201, USA (zoheyr.doctor@gmail.com)

³ Kavli Institute for Cosmological Physics, The University of Chicago, 5640 South Ellis Avenue, Chicago, Illinois 60637, USA

⁴ Enrico Fermi Institute, The University of Chicago, 933 East 56th Street, Chicago, Illinois 60637, USA (michael.j.zevin@gmail.com)

⁵ Helmholtz-Institut für Strahlen- und Kernphysik (HISKP), Nussallee 14-16, D-53115 Bonn, Germany (sambaran.banerjee@gmail.com)

⁶ Argelander-Institut für Astronomie (AIfA), Auf dem Hügel 71, D-53121 Bonn, Germany

⁷ Gravity Exploration Institute, School of Physics and Astronomy, Cardiff University, Cardiff, CF24 3AA, UK
(chattopadhyaydebatri@gmail.com)

Draft version August 17, 2022

ABSTRACT

The LIGO-Virgo-KAGRA (LVK) Collaboration has reported nearly 100 BH-BH mergers. The LVK provides estimates of rates, masses, effective spins, and redshifts for these mergers. Yet, the formation channel(s) of the mergers remains uncertain. One way to search for a formation site is to contrast properties of detected BH-BH mergers with different models of BH-BH merger formation. Our study is designed to investigate the usefulness of the total BH-BH merger mass and its evolution with redshift in establishing the origin of gravitational-wave sources. We find that the average *intrinsic* BH-BH total merger mass shows exceptionally different behavior for the models that we adopt for our analysis. In the local universe ($z = 0$) the average merger mass changes from $\overline{M}_{\text{tot,int}} \sim 25 M_{\odot}$ for CE binary evolution and open clusters formation channels, to $\overline{M}_{\text{tot,int}} \sim 30 M_{\odot}$ for the stable-RLOF binary channel, to $\overline{M}_{\text{tot,int}} \sim 45 M_{\odot}$ for the globular cluster channel. These differences are even more pronounced at larger redshifts. However, these differences are diminished when considering LVK O3 detector sensitivity. Comparison with LVK O3 data shows that none of our adopted models can match the data despite large errors on BH-BH masses and redshifts. We emphasize that our conclusions are derived from a small set of 6 models that are subject to numerous known uncertainties. We also note that BH-BH mergers may originate from a mix of several channels and that other (than those adopted here) BH-BH formation channels may exist.

Subject headings: stars: black holes, neutron stars, x-ray binaries

1. INTRODUCTION

The latest LIGO-Virgo-KAGRA (LVK) Collaboration catalog, GWTC-3 (The LIGO Scientific Collaboration et al. 2021a), reports the detection of 90 double compact object mergers, 83 of which are confidently classified as binary black hole mergers. The LVK Collaboration also provided estimates of the intrinsic population properties of these mergers such as their distributions of rates, masses, and effective spins. The merger rate density of BH-BH systems at a fiducial redshift of $z = 0.2$ is $17.3 - 45 \text{ Gpc}^{-3} \text{ yr}^{-1}$ and the rate increases with redshift (The LIGO Scientific Collaboration et al. 2021c). Masses of BH-BH mergers show complex multi-feature behavior (Tiwari & Fairhurst 2021; Edelman et al. 2022; The LIGO Scientific Collaboration et al. 2021c). BH-BH merger effective spins are mostly positive and small ($0 < \chi_{\text{eff}} < 0.3$) with $\sim 10 - 30\%$ contribution of mergers with high positive ($\chi_{\text{eff}} > 0.3$) effective spins (Roulet et al. 2021; Abbott et al. 2021; Abbott et al. 2021).

Despite all the available information and rapidly increasing number of detected BH-BH mergers, their origin and specific formation mechanism is not known. Several formation channels are under close investigation, each corresponding to a specific formation site of BH-BH mergers and specific evolutionary processes involved

in the evolution of BH-BH progenitors. Evolution of binary systems in isolation (galactic fields) can provide ample resources for BH-BH merger formation via several sub-channels; evolution that involves a common envelope phase (CE, e.g., Belczynski et al. 2016a; Giacobbo & Mapelli 2018; Kinugawa et al. 2020; García et al. 2021), evolution that only requires binary interactions through stable Roche-lobe overflow (RLOF, e.g., van den Heuvel et al. 2017; Neijssel et al. 2019a; Bavera et al. 2021; Olejak et al. 2021), and chemically homogeneous evolution that requires rapidly rotating stars (e.g., Marchant et al. 2016; de Mink & Mandel 2016; Mandel & de Mink 2016). Evolution of objects in dense stellar systems may also provide satisfactory conditions for dynamical formation of BH-BH mergers; in young open clusters (e.g., Banerjee (2018a); Di Carlo et al. (2020); Kremer et al. (2020); Rastello et al. (2021); Chattopadhyay et al. (2022)), in dense globular cluster (e.g., Rodriguez et al. 2016b; Askar et al. 2017; Antonini & Gieles 2020), and in massive nuclear clusters (e.g., Arca-Sedda & Capuzzo-Dolcetta 2017; Arca Sedda 2020; Fragione et al. 2021; Mapelli et al. 2021). There are also formation channels that bridge the two above major classes of isolated and dynamical BH-BH formation. Multiple systems, in particular triples and quadruples, are also esti-

mated to produce BH-BH mergers through combination of typical stellar evolution assisted by dynamical interactions of stars (e.g., Antonini et al. 2017; Safarzadeh et al. 2020). Alternatively, gas assisted evolution in AGN disks may provide a way to form merging BH-BH systems (e.g., Samsing et al. 2020; Ford & McKernan 2021).

Identifying the actual BH-BH merger formation channel or channels is hindered by numerous modeling uncertainties (Arca Sedda & Benacquista 2019; Belczynski et al. 2022; Broekgaarden et al. 2021; Gallegos-Garcia et al. 2021). For example, merger rates for double compact objects vary by orders of magnitude for each formation channel (e.g., Mandel & Broekgaarden 2021), while predicted mass distributions are extremely sensitive to various model assumptions (e.g., Olejak et al. 2021). Ideally, a given model should fit all physical properties (rates, masses, spins) for all three double compact object types (BH-BH/BH-NS/NS-NS mergers; NS: neutron star). Before this is accomplished, we need to build understanding of how various model parameters change properties of double compact objects within various formation channels. Numerous studies were already dedicated to merger rates, NS/BH spins, or compact object masses (e.g., Timmes et al. (1996); Lipunov et al. (1997); Belczynski et al. (2002); Voss & Tauris (2003); Podsiadlowski et al. (2003); Zampieri & Roberts (2009); O’Connor & Ott (2011); Dominik et al. (2012a); Mapelli (2016); Arca Sedda et al. (2018); Stevenson et al. (2019); Spera et al. (2019); Olejak & Belczynski (2021); van Son et al. (2021); Ford & McKernan (2021); Broekgaarden et al. (2021)). Many of the above studies present BH-BH merger masses, but the evolution of mass with redshift is usually not shown nor discussed in detail. One notable exception is work by van Son et al. (2022) who present detailed analysis of primary (more massive) BH mass and its evolution with redshift for BH-BH mergers for two (RLOF and CE) sub-channels of isolated binary evolution. None, however, have focused on average total BH-BH mass and its evolution with redshift. Here we present and discuss the cosmic evolution of average total mass of BH-BH mergers arising from various evolutionary channels. We note that empirical studies have been performed to assess changes in the BH-BH mass distribution shape with redshift, but thus far no definitive evidence of such mass distribution evolution has been found (Fishbach et al. 2021; Tiwari 2022; The LIGO Scientific Collaboration et al. 2021c).

2. MODELS OF BH-BH FORMATION

2.1. Isolated Binary Evolution Models

We use three models of BH-BH formation from isolated binary stars that were calculated with the `StarTrack` population synthesis code (Belczynski et al. 2002, 2008). The standard evolution involves evolution of massive binary stars with empirically derived initial conditions (Sana et al. 2012; de Mink & Belczynski 2015). In particular, for massive stars the initial mass function (IMF) is adopted to be a power-law ($\propto M^{-2.3}$) and it extends to initial star mass of $150 M_{\odot}$. Input physics includes wind losses for massive stars: O/B star and WR-type winds in addition to LBV winds (Vink et al. 2001; Belczynski et al. 2010a). We treat the accretion onto compact objects during RLOF and from stellar winds using ap-

proximations presented by King et al. (2001); Mondal et al. (2020). CE evolution is treated with the energy balance prescription of Webbink (1984) and we limit accretion onto compact objects during a CE phase to 5% of the Bondi rate (MacLeod et al. 2017). We employ two models of core-collapse supernova (SN) engine in NS/BH mass calculation (Fryer et al. 2012) that either allow (delayed SN engine) or do not allow (rapid SN engine) for filling in the lower mass gap (the dearth of compact objects with mass $\sim 2-5 M_{\odot}$) with compact objects between NSs and BHs (Belczynski et al. 2012; Zevin et al. 2020). We assume the minimum BH mass of $2.5 M_{\odot}$. In fact, we use the updated variants of rapid and delayed SN engines from Olejak et al. (2022). This study allows for gradual filling of the lower mass gap with compact objects through a single parameter: f_{mix} . Isolated binary models employ either $f_{\text{mix}} = 0.5$ (close to original delayed SN engine) and $f_{\text{mix}} = 4.0$ (close to the original rapid SN engine). For simplicity, when discussing binary models we will refer to them as having delayed or rapid SN engine physics. Pulsational pair-instability SNe (PPSN) and pair-instability SNe (PSN) are assumed to be weak and allow for the formation of BHs with mass up to $\sim 55 M_{\odot}$ (Leung et al. 2019; Belczynski et al. 2020). We use the fallback-decreased NS/BH natal kicks with $\sigma = 265 \text{ km s}^{-1}$ (Hobbs et al. 2005), and do not allow CE survival for Hertzsprung gap donors (Belczynski et al. 2007). The results of population synthesis calculations are post-processed with Madau & Fragos (2017) star formation rate history in Universe and with evolving with redshift metallicity distribution for Population I/II stars as presented in Belczynski et al. (2020) to allow calculation of BH-BH merger population for redshift range $z = 0-15$.

The standard physics presented above produces a majority of BH-BH mergers through the classical (CE) isolated binary evolution channel. In this channel, binaries that undergo RLOF with a donor star that is approximately twice the mass of the accretor or more ($q \gtrsim 2$) are subject to CE evolution that leads to orbital decay, and may lead to BH-BH merger under favorable conditions. We adopt model M380.B from Olejak et al. (2021) that produces 99.5% of BH-BH mergers through CE evolution. Delayed SN engine is employed in this model.

In our second model, we adopt non-standard CE development criteria that allows for stable RLOF to proceed even for systems with donors as massive as eight times mass of the accretor ($q \lesssim 8$; Pavlovskii et al. 2017). Such evolution, also under favorable conditions, may lead to orbital decay and formation of BH-BH merger (van den Heuvel et al. 2017). We adopt model M480.B from Olejak et al. (2021) that produces 94% of BH-BH mergers through stable RLOF evolution (and the rest through CE). Delayed SN engine is employed in this model.

In our third model we adopt standard CE development criteria, but extend the IMF to $200 M_{\odot}$ and allow for less restrictive PPSN/PSN limits on BH mass. It was argued that it is possible that the upper BH mass gap is located in a different place on BH mass spectrum or may not exist at all (Farmer et al. 2020; Costa et al. 2021; Farrell et al. 2021). We adopt a model presented by Belczynski (2020) that avoids PPSN mass loss for helium core masses up to $M_{\text{He}} < 90 M_{\odot}$, with stars above this mass

threshold destroyed by PSNe. This allows for formation of BHs with mass up to $90 M_{\odot}$ from low-metallicity stars. Delayed SN engine is employed in this model.

In our fourth model we adopt exactly the same input physics as in the third model, but we employ the rapid SN engine instead.

This sequence of models with specific choices of input physics was design to show the dependence of total BH-BH merger mass on some of the most important and most uncertain parts of stellar and binary physics employed in our isolated binary evolution models.

2.2. Globular Cluster Dynamical Models

We use globular cluster models from the BH-BH formation channel analysis of Zevin et al. (2021), which have data relevant to this work publicly available on Zenodo (Zevin 2020). These models originate from a grid of 96 N -body models of collisionless star clusters simulated using the Hénon-style cluster Monte Carlo code CMC (Hénon 1971; Hénon 1971; Joshi et al. 2000; Pattabiraman et al. 2013), as described in Rodriguez et al. (2019). Cluster birth times and cluster initial metallicity follow cosmological models for globular cluster formation (El-Badry et al. 2019), as outlined in (Rodriguez & Loeb 2018) and Rodriguez et al. (2018a). In particular, clusters with three metallicities are used $Z = 0.005, 0.001, 0.0002$. The initial binary fraction for stars born in these cluster models is set to 10% and is independent of stellar mass; the true value for the binary fraction of stars born in globular clusters is observationally unconstrained.

Stars and binaries that are born in GCs are evolved with rapid evolutionary formulas (Hurley et al. 2000, 2002) with updated prescriptions for stellar winds, compact object masses, and supernova natal kicks (see Rodriguez et al. 2016a, 2018b). Initial masses of single stars and primaries in binary systems are taken from a Kroupa IMF ($\propto M^{-1.3}$, in the range $0.08 - 0.5 M_{\odot}$ and $\propto M^{-2.3}$, in the range $0.5 - 150 M_{\odot}$), with secondary components in binaries drawn from a uniform mass ratio distribution. Semimajor axes of initial binaries are drawn flat in $\log(P(a)da \propto 1/a)$ between the point of stellar contact and the hard-soft boundary, where the orbital velocity of the binary equals the typical velocity of particles in the cluster (for a typical velocity of 10 km s^{-1} this translates to $\sim 1 - 5 \times 10^5 R_{\odot}$ for equal-mass binaries with component mass between $30 M_{\odot}$ and $150 M_{\odot}$). Eccentricities are drawn from a thermal distribution ($p(e)de = 2ede$). Stellar winds for massive stars are adopted from Vink et al. (2001) during the main sequence and from Vink & de Koter (2005) for naked helium stars, with later evolutionary stages following Belczynski et al. (2010a). Compact object masses are calculated based on 1-D supernova models that allow for fallback and direct BH formation, with a rapid supernova engine that produces a lower mass gap between NSs and BHs (Fryer et al. 2012). Note that for isolated binary evolution BH-BH formation we employed models with delayed SN engine. However, as we show in Section 3.1 the choice of SN engine model does not impact average total BH-BH merger mass and its evolution with redshift. Massive stars (with He cores above $45 M_{\odot}$ are subject to PPSN/PSN and stellar-origin natal BH mass is limited to $\lesssim 45 M_{\odot}$. BH natal kicks are taken from a Maxwellian distribution with

1-D $\sigma = 265 \text{ km s}^{-1}$, and kicks are decreased by fallback (i.e., no natal kicks for massive BHs that form through direct core collapse). This set of models assumes that BHs are born with near-zero spin due to highly efficient angular momentum transport (e.g., Fuller & Ma 2019; Qin et al. 2018; Belczynski et al. 2020). Spin-up of massive stars (BH progenitors) by tidal interactions in close binaries is not taken into account. Stars (90%) and primordial binaries (10%) in each cluster form the first generation of BHs (with masses limited to $\lesssim 45 M_{\odot}$).

Dynamical interactions and also mergers of BH-BH systems formed from primordial binaries produce future generations of BHs. Obviously, these BHs can be more massive than the first generation of BHs. The second generation of BHs is typically formed with high spins ($a \sim 0.7$) due to the angular momentum of the pre-merger double compact object orbit. Spins of the BH remnant are calculated using the precession package (Gerosa & Kesden 2016), as described in Rodriguez et al. (2018a). Asymmetries in the BH components of the merger (unequal masses, spins) will lead to a dispersion of spin magnitudes around $a \sim 0.7$. Some second-generation BHs receive gravitational-wave recoil kicks that may remove BHs from clusters, though since the models we consider assume BHs are born with negligible spin, almost $\sim 60\%$ of second-generation BHs are retained since recoil kicks depend then entirely on mass ratio and are typically $\lesssim 100 \text{ km s}^{-1}$ (Rodriguez et al. 2019). Those that remain bound continue to contribute to cluster evolution and to GC BH-BH merger populations. Due to the relatively low escape velocities of globular clusters ($\sim 30 - 100 \text{ km s}^{-1}$), higher-generation merger products are typically ejected from the cluster via gravitational-wave recoil kicks due to their components having large spins as a result of their formation from previous BH-BH mergers; $\lesssim 0.1\%$ mergers containing a second-generation BH remain bound to the cluster (Rodriguez et al. 2019).

2.3. Open Cluster Dynamical Models

In this work, the long-term N -body evolutionary model set of star clusters as described in Banerjee (2021c) is utilized. The computed models are described in detail in Banerjee et al. (2020); Banerjee (2021b,c) and are summarized below.

The model star clusters, initially, have mass within $2 \times 10^4 M_{\odot} \leq M_{\text{cl}} \leq 10^5 M_{\odot}$, size (half-mass radius) $1 \text{ pc} \leq r_{\text{h}} \leq 2 \text{ pc}$, and metallicity $0.0001 \leq Z \leq 0.02$, and they are subjected to a solar-neighborhood-like external galactic field. The initial models are composed of ZAMS stars of masses $0.08 M_{\odot} \leq m_{*} \leq 150.0 M_{\odot}$ that are distributed according to the standard IMF (Kroupa 2001). About half of the models have a primordial-binary population (overall initial binary fraction $f_{\text{bin}} \approx 5\%$ or 10%) where all O-type stars (stars with ZAMS mass $\geq 16 M_{\odot}$) are paired among themselves (i.e, initial binary fraction among O-type stars is $f_{\text{Obin}} = 100\%$) following an observationally-deduced distribution of massive-star binaries (Sana & Evans 2011; Sana et al. 2013; Moe & Di Stefano 2017). Such cluster parameters and stellar membership are consistent with those observed in ‘fully’-assembled, (near-)spherical, (near-)gas-free young massive clusters (YMCs) which evolve into medium-mass open clusters (OCs) (Portegies Zwart et al. 2010). They

continue to form, evolve, and dissolve in the Milky Way and other galaxies (as such, anywhere in the Universe) as a part of the galaxies’ ongoing star formation.

These model clusters evolve due to two-body relaxation (Spitzer 1987), close (relativistic) dynamical encounters (Heggie & Hut 2003, without applying any gravitational softening), and stellar evolution. This is achieved using NBODY7, a state-of-the-art post-Newtonian (PN) direct N-body integration code (Aarseth 2012; Nidadori & Aarseth 2012) that couples with the semi-analytical stellar- and binary-evolutionary scheme BSE (Hurley et al. 2000, 2002). As detailed in Banerjee et al. (2020), the integrated BSE is updated in regards to prescriptions of stellar wind mass loss and formation of NSs and BHs. NSs and BHs form according to the ‘rapid’ or ‘delayed’ core-collapse SN models of Fryer et al. (2012), and the PPSN and PSN models of Belczynski et al. (2016b). The majority of the computed models of Banerjee (2021c) employ the rapid-SN prescription although a few models employ the delayed-SN prescription, for exploratory purposes. The dynamical evolution and merger outcomes of the clusters are unlikely to be significantly affected by this difference, as discussed in Banerjee et al. (2020); Banerjee (2020).

A newly formed NS or BH receives a natal kick that is modulated based on SN matter fallback onto it, as in Belczynski et al. (2008). The adopted fallback model is that of Fryer et al. (2012). For all core-collapse SN remnants, the ‘base’ natal kick is assigned from a Maxwellian distribution with one-dimensional dispersion of $\sigma = 265 \text{ km s}^{-1}$, i.e., the same velocity dispersion as that of the Galactic single NS population (Hobbs et al. 2005). However, due to momentum conservation, the material fallback slows down the remnants, causing BHs of $\gtrsim 10 M_{\odot}$ to be retained in the clusters right after their birth. The material fallback also shapes the mass distribution of NSs and BHs. NSs formed via electron-capture SN (ECS; Podsiadlowski et al. 2004) also receive small natal kicks of a few km s^{-1} (Gessner & Janka 2018) and are retained in the clusters at birth. The present remnant scheme forms first-generation of BHs in the range $\approx 3 - 45 M_{\odot}$ (the upper limit set by PPSN) and exhibits a PSN mass gap between $\approx 45 - 120 M_{\odot}$ (see Fig. 2 of Banerjee et al. 2020). See Banerjee et al. (2020) for further details and the description of the implementations in BSE and NBODY7.

In NBODY7, the PN treatment is handled by the ARCHAIN algorithm (Mikkola & Tanikawa 1999; Mikkola & Merritt 2008). The treatment allows for general relativistic (GR) evolution of the innermost NS- and/or BH-containing binary of an in-cluster (i.e., gravitationally bound to the cluster) triple or higher order compact subsystem, in tandem with the Newtonian-dynamical evolution of the subsystem (Kozai-Lidov oscillation or chaotic three-body interaction), leading to the binary’s (in-cluster) GR in-spiral and potential merger. The PN treatment applies also to the GR evolution of in-cluster NS/BH-containing binaries that are not a part of a higher-order subsystem. As demonstrated in previous studies (Banerjee et al. 2010; Banerjee 2017, 2018b; Rastello et al. 2019; Banerjee 2021b), the moderate density ($10^2 - 10^3 \text{ stars pc}^{-3}$) and velocity dispersion ($\lesssim 10 \text{ km s}^{-1}$) in the model clusters make them efficient

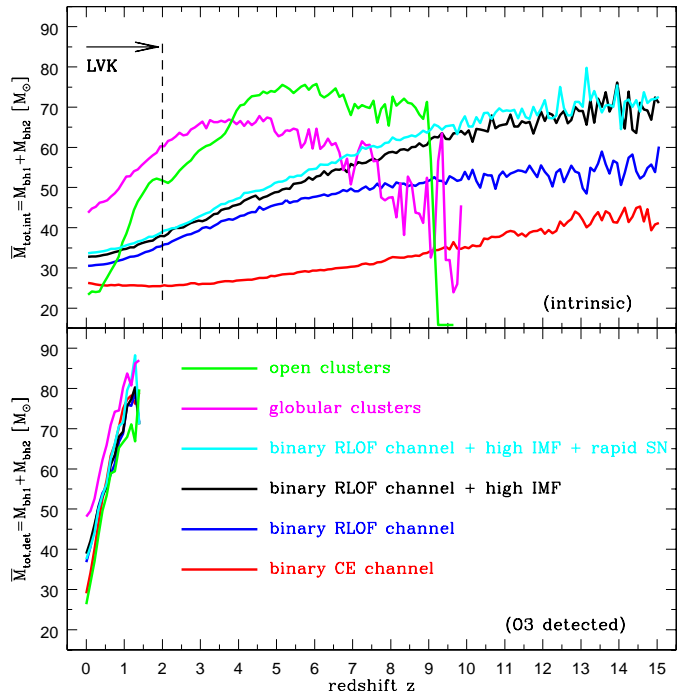


FIG. 1.— Top: intrinsic average total BH-BH merger mass change as a function of redshift for different BH-BH formation channels: globular cluster and open cluster dynamical channels, and CE and RLOF isolated binary evolution channels. For the RLOF channel we show three variations: first allows for stars to form to $150 M_{\odot}$ and PPSN/PSN limit BH masses to $\sim 55 M_{\odot}$, second allows for star formation to $200 M_{\odot}$ and PPSN/PSN limit BH masses to $90 M_{\odot}$, while third is the same as the second variation but employs rapid SN engine (all other isolated binary models employ delayed SN engine). We show the approximate redshift range for design (future) LIGO/Virgo/KAGRA detection of BH-BH mergers (the range for Einstein Telescope and Cosmic Explorer covers entire plot). Bottom: detected average total BH-BH merger mass as a function of redshift. The gravitational-wave instrumental and observational selection effects are applied to the models from the top panel to show which BH-BH mergers may be currently (O3 sensitivity of LVK) detectable. Note that rather different intrinsic curves (top), become almost indistinguishable when detection biases are applied (bottom).

in dynamically assembling PN subsystems, particularly, those composed of BHs. On the other hand, the clusters’ low escape speed ($\sim 10 \text{ km s}^{-1}$) causes the dynamically-ejected BH-BH systems to be typically wide (Portegies Zwart & McMillan 2000), with a GR inspiral time (Peters 1964) often exceeding the Hubble time. These cause the majority of the GR mergers from these computed clusters to be in-cluster BH-BH mergers.

In the computed models, star-star and star-remnant mergers happen due to evolution of massive primordial binaries and three-body interactions. In the present models, a star-star merger results in the loss of $\approx 10\%$ of the total merging mass as suggested by hydrodynamical calculations (J. C. Lombardi et al. 2002; Gaburov et al. 2008). In a BH-star merger (forming a BH-Thorne-Zytkow Object, BH-TZO), $\approx 90\%$ of the star’s mass is taken to be accreted onto the BH. The model grid used in this work comprises 74 long-term ($\sim 10 \text{ Gyr}$) evolutionary cluster models (see Table A1 of Banerjee 2021c).

3. RESULTS

3.1. Evolutionary Analysis

Our main result is shown in the top panel of Figure 1. It shows evolution of the average intrinsic (not redshifted nor detection weighted) total BH-BH mass ($\overline{M}_{\text{tot,int}} = M_{\text{bh1}} + M_{\text{bh2}}$) with redshift (z). The evolution is shown for the six models (see Sec. 2) of BH-BH merger formation: the globular cluster dynamical channel, the open cluster dynamical channel, the classical CE isolated binary evolution channel, the RLOF isolated binary evolution channel, the extended RLOF channel (with more massive stars and BHs), and the extended RLOF channel with rapid SN engine.

Within the approximate LIGO-Virgo-KAGRA design redshift range for detection of BH-BH mergers ($z < 2$)¹, the CE channel produces the lowest mass BH-BH mergers ($\overline{M}_{\text{tot,int}} \sim 25 M_{\odot}$, irrespective of the redshift), the three RLOF channels produce more massive BH-BH mergers that show a slow increase of the average mass with increasing redshift as the metal-poor environments at higher redshifts produces more massive BHs ($\overline{M}_{\text{tot,int}} \sim 30 \rightarrow 35 M_{\odot}$ for $z = 0 \rightarrow 2$), and the globular cluster channel produces the most massive BH-BH mergers with fast increase of the average mass with redshift ($\overline{M}_{\text{tot,int}} \sim 45 \rightarrow 60 M_{\odot}$ for $z = 0 \rightarrow 2$). The open cluster channel generates the most dramatic evolution of the intrinsic average total BH-BH merger mass ($\overline{M}_{\text{tot,int}} \sim 25 \rightarrow 50 M_{\odot}$ for $z = 0 \rightarrow 2$).

In the entire presented redshift range ($z < 15$) that will be accessible to Einstein Telescope and Cosmic Explorer, the four isolated binary evolution channels produce gradually more massive BH-BH mergers with increasing redshift (at $z = 15$ we find: $\overline{M}_{\text{tot,int}} \sim 40 M_{\odot}$ for the CE channel, $\overline{M}_{\text{tot,int}} \sim 55 M_{\odot}$ for the RLOF channel, and $\overline{M}_{\text{tot,int}} \sim 70 M_{\odot}$ for both RLOF channels with extended IMF). For BH-BH mergers in the globular cluster channel, we find that the average mass first increases with redshift (reaching a maximum of $\overline{M}_{\text{tot,int}} \sim 65 M_{\odot}$ at $z = 3 - 5$) and then gradually decreases with increasing redshift. For the open cluster channel, we find that the average BH-BH mass first increases with redshift, reaching high values ($\overline{M}_{\text{tot,int}} \sim 70 M_{\odot}$ at $z = 4 - 9$) and then sharply decreases for higher redshifts.

The general increase of the intrinsic average BH-BH mass with redshift for all four isolated binary evolution channels is easily understood in the framework of cosmic chemical evolution. The chemical composition of stars (i.e., metallicity Z) is the primary factor setting the mass of stellar-origin BHs (Belczynski et al. 2010a). At lower metallicities, stellar winds are weaker (which removing mass from stars), and more massive BHs are able to form. Since metallicity decreases with redshift, more massive stellar-origin BHs form at higher redshifts. There is an exception from this general trend for the CE BH-BH formation channel at low redshifts ($z \lesssim 2 - 3$), where the BH-BH merger total mass remains constant and does not change with redshift. We explain this behavior in Section 5.

The lowest average total BH-BH merger mass (at any redshift) is found for the CE BH-BH binary formation

channel. The actual value of the average mass is a combination of the adopted stellar wind mass loss for massive stars and their dependence on metallicity, the cosmic evolution of metallicity with redshift, and the specific evolutionary sequences (set by stellar/binary input physics assumptions) producing BH-BH mergers in the CE binary channel. The RLOF binary channel produces on average more massive BH-BH mergers. Since for this channel wind mass loss and cosmic metallicity evolution are the same as for the CE channel, the entire difference in average total mass originates from different stellar/binary evolutionary assumptions. We explain the (non-trivial) origin of this difference in Section 6. Finally, the two RLOF models with high (extended) IMF naturally produce the most massive BH-BH mergers among our isolated binary models. In these two models, BHs may form up to $90 M_{\odot}$ as compared to maximum mass of a BH of $\sim 55 M_{\odot}$ in the other two binary models. We note slightly larger total BH-BH masses (\lesssim few M_{\odot}) for model with the rapid SN engine as the BHs that would form in the lower mass gap in the delayed SN engine model are simply forming with masses just above the mass gap. Note that the small differences between these two models with extended IMF but with different SN engines are much smaller than differences associated with the BH-BH formation mode (CE versus RLOF channels) or the change of IMF and PPSN/PSN model.

The globular cluster channel produces on average significantly more massive BH-BH mergers at low and intermediate redshifts ($z < 5$) compared to any presented isolated binary evolution model by about $\overline{M}_{\text{tot,int}} \sim 10 - 20 M_{\odot}$ (see Fig. 1). This is due to the most massive BHs in the cluster more readily synthesizing binaries through dynamical interactions, as well as the contribution of mergers containing a second-generation BH that was retained in the cluster following its first merger. The average total merger mass drops at high redshifts ($z \gtrsim 7$) when GC BH-BH mergers become more dominated by BH-BH mergers from primordial binaries.

Unlike the isolated evolution channels considered, the globular cluster model has a peak in the average mass of BH-BH mergers near the peak of globular cluster formation, at redshifts of $z \sim 3 - 5$. The most massive BHs in the cluster ($\gtrsim 20 M_{\odot}$) are typically the first to be dynamically processed, either merging in the cluster at early times or being ejected and inspiraling over longer timescales. Less massive BHs born in the clusters ($\sim 10 - 15 M_{\odot}$) follow suit and typically merge at later times than their more massive counterparts, leading to the decrease in the average total mass lower redshifts ($z \lesssim 3$). At $z \gtrsim 5$, primordial binaries in the cluster that evolve and lead to BH-BH mergers formed in quasi-isolation (without much assistance from dynamical interactions) have a larger contribution to the total population of BH-BH mergers, driving the overall decline in the average mass at large redshifts. These systems rapidly merge on timescales shorter than the mass segregation timescale in their GC hosts of $\mathcal{O}(100 \text{ Myr})$. However, dynamically processed mergers still occur at these higher redshifts, which combined with small number statistics (GCs are just beginning to form) leads to the fluctuating behavior in the average total mass evolution at $z \gtrsim 5$. The relative contribution of BH mergers

¹ The maximum detectable redshift of a $50M_{\odot}$ - $50M_{\odot}$ BH merger with Advanced LIGO at design sensitivity is $z_h = 1.9$, as calculated with the gravitational wave distance calculator described in Chen et al. (2021).

from quasi-isolated evolution prior to the peak of globular cluster formation and their impact on the average mass change with redshift depends on the metallicity evolution of cluster formation, which is distinct from the metallicity evolution of isolated binaries in galactic fields.

Interpretation along lines similar to the case of GCs applies to the evolution of the average total mass with merger redshift for OCs (Figure 1; top panel). However, a twist for OCs is that such systems, being 1-2 orders of magnitude less populous than but of similar (initial) length scale as GCs, have a factor of a few to tens shorter two-body relaxation time (Spitzer 1987) compared to GCs. In OCs, the most massive BHs/BH-progenitors segregate to the cluster center in $\lesssim 10$ Myr (see Banerjee 2021a). Also, before the formation of BHs, a fraction of the BH progenitors already undergo complete mass segregation due to the shorter relaxation/mass-segregation timescale. These cause the dynamical processing and mergers among BHs to commence at earlier ages (i.e. at larger redshifts) and closer to the quasi-isolated mergers in OCs than in GCs. Also, due to the smaller member number and hence primordial-binary population in OCs, the models produce a much smaller number of quasi-isolated BH-BH mergers per cluster than the GC models (Fragione & Banerjee 2020).

The effects of these differences in OCs can be seen in Figure 1. As opposed to GCs, $\overline{M}_{\text{tot,int}}$ for OCs rises sharply at $z \approx 9$ (fewer quasi-isolated mergers), thereafter remaining nearly flat and peaking weakly in between $5 < z < 6$ (pre/faster mass segregation), and drops off towards low z faster than GCs (faster dynamical processing due to shorter relaxation times in OCs). It is also to be noted that the OCs are taken to follow a different metallicity-dependent cosmic star formation history (Chruslinska & Nelemans (2019) their 'moderate-Z' relation; see Banerjee (2021c) for the details) than those for both the isolated-binary and GC models presented here, which would also cause differences in the redshift dependence of $\overline{M}_{\text{tot,int}}$. Although OCs are inefficient in producing massive BHs via hierarchical mergers, the computed OC models adopt a small, $\approx 10\%$, mass loss in star-star mergers (based on hydrodynamic stellar merger calculations; see Sec. 2.3), which is the main channel for forming the most massive BHs lying within the PPSN/PSN mass gap in these models (Banerjee 2021b,a). Furthermore, a 90% BH-TZO accretion is adopted (Sec. 2.3). These, along with the tendency of having lower metallicity at high redshifts than globular cluster or binary models, results in a higher maximum $\overline{M}_{\text{tot,int}}$ for OCs (Figure 1).

3.2. Comparison to Observed Gravitational Waves

Although all models explored in this work show notable differences in the average total mass of mergers and its evolution with redshift (the only exception being the two RLOF models with extended IMF: one with rapid and one with delayed SN engine), there is no guarantee these differences can be measured with current gravitational-wave sensitivity. Firstly, gravitational-wave sources are subject to strong selection effects, which not only limit the distance to which BH-BH mergers can be detected, but also preferentially enable detection of certain binary mass and spin configurations. As a result, the properties

of the detected population of BH-BH mergers will not match those of the intrinsic population. Furthermore, gravitational-wave detectors are subject to a variety of sources of noise, so the true masses, spins, and distances of detected events can only be estimated, often with sizable uncertainties. Finally, we are still in the era of small number statistics when it comes to gravitational-wave detections, so even if the true properties of a detected system were known, there still exists a counting uncertainty in the number of similar events occurring in the Universe.

Given these combined effects as well as the poorly understood systematic uncertainties in the six population synthesis models presented here, we take a simple approach to assessing whether these models are distinguishable with current detections, and whether any of them are a reasonable fit to the data, in analog to the investigations in Fishbach et al. (2021). In Figure 2, we show the average *detected* mass $\overline{M}_{\text{tot,det}}$ as a function of redshift under each of our six models by computing the average detected total mass in 14 equally spaced redshift bins (i.e. 15 bin edges) from $z = 0$ to $z = 1.5$. These curves are also reproduced in Figure 1 for comparison to the intrinsic average masses. $\overline{M}_{\text{tot,det}}$ is essentially $\overline{M}_{\text{tot,int}}$ filtered through the LVK detector and analysis selection function. To simulate these effects of the detector and analysis selection bias on the detected populations, we reweight the detected software injections provided in The LIGO Scientific Collaboration et al. (2021c) by the intrinsic simulated populations. To perform the re-weighting, a histogram of the population synthesis samples from each model is used to approximate the intrinsic simulated population probability distribution over masses and redshifts.

The model curves in Figure 2 show the average detected total mass increasing as a function of redshift, which is expected given that less-massive sources are detectable out to lower redshifts than the more massive sources. The rate of change of the average detected total mass with redshift is approximately the same for all our models, though the CE channel shows the strongest increase with redshift. To compare these curves to those in Figure 1, consider that the slopes of the $\overline{M}_{\text{tot,det}}$ lines are strongly influenced by the selection effects, which will increase the lowest detectable mass with increasing redshift and therefore force models with low, constant intrinsic average mass like the CE channel to appear to evolve with redshift in the detected population. In contrast, for the open clusters, the average intrinsic mass changes from ~ 25 to $\sim 50M_{\odot}$ between redshift 0 and 1 which matches what is seen in the detected average mass. This means that the true average mass evolution with redshift in the open cluster model is roughly following the O3 LVK selection effects. The similarity between slopes of the $\overline{M}_{\text{tot,det}}$ curves suggests that the changes in the total mass distribution mean over redshift is not a good distinguisher of these models given current sensitivity. However, the overall mass scale is more telling: the GC model predicts a higher average detected mass than the other models by $\sim 10 - 20M_{\odot}$, regardless of redshift.

To compare these simulated average detected masses to the masses of detected BH-BHs, in gray we overlay

the 90% credible regions on detector-frame total mass and redshift for the BH-BH systems in GWTC-3 from the third LVK observing run (Abbott et al. 2021; Abbott et al. 2021; The LIGO Scientific Collaboration et al. 2021a). Only BH-BH mergers from O3 are selected for uniform sample. The credible regions are generated via kernel density estimates (KDEs) of posterior samples provided by the LVK, re-weighted to a prior that approximates empirical measurements of the merger population distribution (The LIGO Scientific Collaboration et al. 2021c; Roulet et al. 2021; The LIGO Scientific Collaboration et al. 2021b). Specifically, we use (1) a broken power law prior on the more massive BH in the binary’s mass, with $p(m_1) \propto m_1^{-1.7}$ for $m_1 < 40M_\odot$, and $p(m_1) \propto m_1^{-5}$ for $m_1 \geq 40M_\odot$, (2) a $p(q) \propto q$ prior for the mass ratio q , and (3) a uniform-in-comoving-time-volume prior on z , i.e. $p(z) \propto \frac{dV}{dz} \frac{1}{1+z}$. Additionally, we estimate the mean mass of these detections over redshift by computing a single total-mass mean from the combined samples of all events in the same redshift bins used for the six models’ curves. We show this estimate in gray in Figure 2.

At $z \sim 0.5$, all the models appreciably under-predict the estimated mean detected mass by $\sim 25M_\odot$, except GC, which underpredicts by $\sim 10M_\odot$. This is consistent with the fact that the GC model is the only model with a non-negligible fraction ($> 1\%$) of systems with $M_{\text{tot,int}} > 100M_\odot$ below $z = 1$. At the highest redshifts, it is not clear which model(s) may fit the data well given that there are few events detected at these distances, and those events have large uncertainties and low significance. At redshifts less than ~ 0.2 , all the models over-predict the average detected mass. This is simply because none of the models predict a sufficiently high rate of low-mass mergers. Overall, these findings, especially at low masses and redshifts, suggest that none of these models alone (or even a mixture of them), are a good fit to GWTC-3 events. However, the GC model offers the closest $\bar{M}_{\text{tot,det}}$ prediction for high redshift events, but would require either a different set of input physics or another channel also with a different set of input physics than explored in this work to fill in the low and high ends of the mass distribution.

We emphasize that the explorations here are primarily illustrative. None of the models herein have been tuned to fit the LVK data, nor have we performed a simultaneous fit to all binary parameters in the LVK catalog accounting for measurement uncertainties. However, comparisons such as the one shown in Figure 2 will be invaluable for assessing the viability of BH-BH formation channel models and enable a narrowing of the parameter space for easier follow-up studies that perform a complete statistical analysis.

4. CONCLUSIONS

We have employed several BH-BH merger formation models to show evolution of the average intrinsic and detected total BH-BH merger mass with redshift. Our main result is shown in Figures 1 and 2. In our analysis we have included the classical isolated binary CE evolution formation channel, three stable RLOF channels: one with a standard IMF (stars with masses $< 150 M_\odot$ and PPSN/PSN limiting BH masses to $< 55 M_\odot$), and two with an extended IMF (stars with masses $< 150 M_\odot$

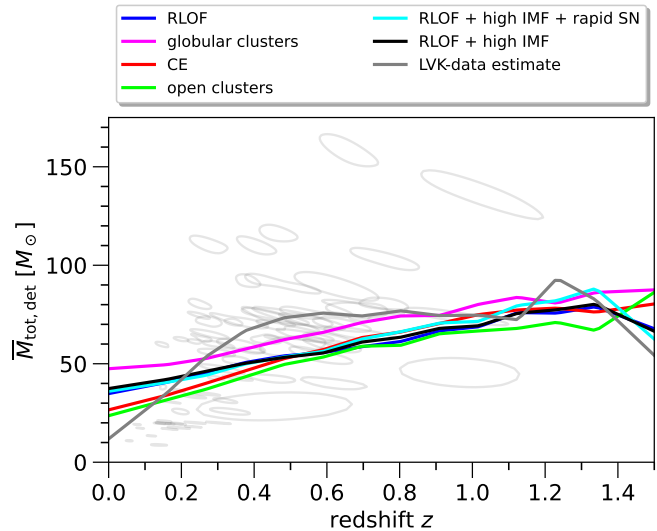


FIG. 2.— The average detected total mass as a function of redshift for the six models considered in this work. The models are overlaid on the gray 90% credible interval parameter regions for BH-BH mergers from LVK O3, re-weighted to an astrophysically realistic prior. The gray line shows an estimate of the mean detected total mass of these events in different redshift bins for all posterior samples under the aforementioned prior.

and PPSN/PSN limiting BH masses to $< 90 M_\odot$) but with different SN engines (delayed and rapid), and globular cluster and open cluster dynamical BH-BH formation channels.

The model differences in average intrinsic BH-BH total mass are both quantitative and qualitative. The lowest average masses are produced by the CE binary channel ($\bar{M}_{\text{tot,int}} \sim 25 M_\odot$ at $z = 0 - 2$), with somewhat larger masses found for RLOF channels ($\bar{M}_{\text{tot,int}} \sim 30 M_\odot$ at $z = 0$ and increasing to $\sim 35 M_\odot$ at $z = 2$). The largest masses in LIGO/Virgo/KAGRA range are produced by globular clusters ($\bar{M}_{\text{tot,int}} \sim 45 M_\odot$ at $z = 0$ with notable increase to $\sim 60 M_\odot$ at $z = 2$). Open cluster BH-BH mergers show the most pronounced evolution of the average total mass in this redshift range ($\bar{M}_{\text{tot,int}} \sim 25 M_\odot$ at $z = 0$ and $\sim 50 M_\odot$ at $z = 2$), bridging isolated binary and globular cluster models.

These differences become more pronounced for higher redshifts. Isolated binary channels show monotonic increase of the average intrinsic BH-BH merger mass with redshift, with the exception that for the CE channel the average intrinsic mass is constant for low redshifts ($z \lesssim 2 - 3$) and then increases with increasing redshift. A different behavior is found for the globular cluster model, for which the average intrinsic merger mass increases with redshift to $z \sim 4$, and then decreases with redshift. The open cluster model shows similar behavior to the globular cluster model, however the largest intrinsic total BH-BH masses are produced at higher redshifts ($\bar{M}_{\text{tot,int}} \gtrsim 70 M_\odot$ for $z \sim 5 - 9$). These trends are understood in the framework of input physics employed in the models (see Sec. 3.1 for details).

We have shown that not only the formation channel (e.g., isolated binary versus cluster BH-BH formation) significantly affects intrinsic average BH-BH merger mass, but that some parts of highly uncertain input

physics within a given formation channel have big impact. For example, changing CE development criteria for isolated binary evolution channel significantly impacts BH-BH merger formation mode (CE versus RLOF) and the intrinsic total BH-BH merger mass. Similar statement can be made about impact of treatment of PPSN/PSN and the extend of IMF in binary evolution calculations. However, not all input physics is that important for the intrinsic average total BH-BH merger mass and its evolution with redshift. For example, SN engine model that regulates the existence and numbers of compact objects with mass in the lower mass gap ($\sim 2 - 5 M_{\odot}$) does not significantly impacts intrinsic average total BH-BH merger mass. Since all these parts of physics of BH-BH merger formation (CE, SN engine, PPSN/PSN) are highly uncertain we adopted models with various assumptions on parameters regulating these processes.

The evolution of the averaged detected BH-BH merger total mass does not differ as much between formation channels compared to the intrinsic mass (see Fig. 2). The four binary models and the open cluster model show a similar behavior for redshifts in which mergers are currently detected ($z \lesssim 1$). Only the globular cluster model results in moderately heavier detected BH-BH mergers (by $\lesssim 10 M_{\odot}$ for $z \lesssim 1$). This is caused by LVK detection biases that affect different models in different ways (as explained in Sec. 3.2). These differences in mass evolution with redshift are too small to differentiate between models with the current LVK data due to large detection errors. Additionally, none of the employed models matches the average detected BH-BH merger masses over entire BH-BH detectable redshift range. However, the adopted globular cluster model matches the current data better than our isolated binary or open cluster models at moderate redshifts $z \sim 0.5$.

The physics of BH-BH merger progenitors for isolated binary, globular cluster, and open cluster formation channels is still subject to many uncertainties (Belczynski et al. 2022; Santoliquido et al. 2021; Chatterjee et al. 2017; Conroy & Gunn 2010). Major overall uncertainties include the underlying cosmic star formation rate of isolated binaries and stars/binaries in globular and open clusters, and metallicity evolution with redshift (Sharda et al. 2021) within each formation channel (Neijssel et al. 2019b). Basic stellar evolution uncertainties include fusion reaction rates (Fields et al. 2018), mixing in stellar interiors (Zhang 2013), stellar wind mass loss rates (Björklund et al. 2022), radial expansion, and core-collapse/supernova physics (Schneider et al. 2019) associated with compact object formation (Belczynski et al. 2022), as well as initial conditions such as the initial mass function, mass ratio, orbital separation, and eccentricity (Klencki et al. 2018). Binary evolution physics is highly uncertain in its treatment of stellar interactions, whether

these are stable or unstable (CE) RLOF events (Ablimit & Maeda 2018; Dominik et al. 2012b). In modeling of dynamical BH-BH formation unknown initial conditions of globular and open clusters (size, density, binary fractions) along with uncertain outcomes of stellar mergers and BH (natal and gravitational-wave) kicks hinders their predictions.

Keeping these uncertainties in mind, we can deliver only a very limited conclusion. For some choices of input physics in a given BH-BH formation channel (six presented models) we predict that the average intrinsic total BH-BH merger mass evolution with redshift changes from model to model, sometimes in rather significant ways. However, due to BH-BH detection selection effects, small statistics of detected sources, and significant uncertainties in detected BH-BH masses and redshifts, the current LVK O3 data does not enable us to identify any model as fitting the data better than another. Additionally, no models (or their potential combinations) fit the entirety of the data well due to their dearth of low-mass events relative to the detected population. More data from LVK in O4 and O5 may change this conclusion. At this moment, it is clear that the average total mass (and its evolution with redshift) may be very different for various formation models, and this may help in the future to eliminate some models and support others, and guide theoretical work on the physics of BH-BH merger progenitors. The total BH-BH merger mass and its evolution with redshift may provide, along other observables, an extra leverage in search for the BH-BH formation site/channel.

KB and AO acknowledge support from the Polish National Science Center grant Maestro (2018/30/A/ST9/00050). ZD is supported by the CIERA Board of Visitors Research Professorship. Support for MZ is provided by NASA through the NASA Hubble Fellowship grant HST-HF2-51474.001-A awarded by the Space Telescope Science Institute, which is operated by the Association of Universities for Research in Astronomy, Incorporated, under NASA contract NAS5-26555. DC is supported by the STFC grant ST/V005618/1. SB acknowledges support from the Deutsche Forschungsgemeinschaft (DFG; German Research Foundation) through the individual research grant “The dynamics of stellar-mass black holes in dense stellar systems and their role in gravitational-wave generation” (BA 4281/6-1; PI: S. Banerjee). SB acknowledges the generous support and efficient system maintenance of the computing teams at the AIfA and HISKP. This work was initiated and performed in part at Aspen Center for Physics, which is supported by National Science Foundation grant PHY-1607611. This material is based upon work supported by NSF’s LIGO Laboratory which is a major facility fully funded by the National Science Foundation.

REFERENCES

- Aarseth, S. J. 2012, *MNRAS*, 422, 841
 Abbott, R., et al. 2021, *Physical Review X*, 11, 021053
 Abbott, R., et al. 2021, arXiv e-prints, arXiv:2108.01045
 Ablimit, I., & Maeda, K. 2018, *ApJ*, 866, 151
 Antonini, F., & Gieles, M. 2020, *Phys. Rev. D*, 102, 123016
 Antonini, F., Toonen, S., & Hamers, A. S. 2017, *ApJ*, 841, 77
 Arca Sedda, M. 2020, *ApJ*, 891, 47
 Arca Sedda, M., Askar, A., & Giersz, M. 2018, ArXiv e-prints
 Arca Sedda, M., & Benacquista, M. 2019, *MNRAS*, 482, 2991
 Arca-Sedda, M., & Capuzzo-Dolcetta, R. 2017, ArXiv e-prints
 Askar, A., Szkudlarek, M., Gondek-Rosińska, D., Giersz, M., & Bulik, T. 2017, *MNRAS*, 464, L36
 Banerjee, S. 2017, *MNRAS*, 467, 524
 —. 2018a, *MNRAS*, 473, 909

- . 2018b, *MNRAS*, 481, 5123
- Banerjee, S. 2020, *Phys. Rev. D*, 102, 103002
- Banerjee, S. 2021a, arXiv e-prints, arXiv:2109.14612
- . 2021b, *MNRAS*, 500, 3002
- . 2021c, *MNRAS*, 503, 3371
- Banerjee, S., Baumgardt, H., & Kroupa, P. 2010, *MNRAS*, 402, 371
- Banerjee, S., Belczynski, K., Fryer, C. L., Berczik, P., Hurley, J. R., Spurzem, R., & Wang, L. 2020, *A&A*, 639, A41
- Bavera, S. S., et al. 2021, *A&A*, 647, A153
- Belczynski, K. 2020, *ApJ*, 905, L15
- Belczynski, K., Bulik, T., Fryer, C. L., Ruiter, A., Valsecchi, F., Vink, J. S., & Hurley, J. R. 2010a, *ApJ*, 714, 1217
- Belczynski, K., Dominik, M., Bulik, T., O'Shaughnessy, R., Fryer, C. L., & Holz, D. E. 2010b, *ApJ*, 715, L138
- Belczynski, K., Holz, D. E., Bulik, T., & O'Shaughnessy, R. 2016a, *Nature*, 534, 512
- Belczynski, K., Kalogera, V., & Bulik, T. 2002, *ApJ*, 572, 407
- Belczynski, K., Kalogera, V., Rasio, F. A., Taam, R. E., Zezas, A., Bulik, T., Maccarone, T. J., & Ivanova, N. 2008, *ApJS*, 174, 223
- Belczynski, K., Taam, R. E., Kalogera, V., Rasio, F. A., & Bulik, T. 2007, *ApJ*, 662, 504
- Belczynski, K., Wiktorowicz, G., Fryer, C. L., Holz, D. E., & Kalogera, V. 2012, *ApJ*, 757, 91
- Belczynski, K., et al. 2016b, *A&A*, 594, A97
- . 2020, *A&A*, 636, A104
- . 2022, *ApJ*, 925, 69
- Björklund, R., Sundqvist, J. O., Singh, S. M., Puls, J., & Najarro, F. 2022, arXiv e-prints, arXiv:2203.08218
- Broekgaarden, F. S., et al. 2021, arXiv e-prints, arXiv:2112.05763
- Chatterjee, S., Rodriguez, C. L., & Rasio, F. A. 2017, *ApJ*, 834, 68
- Chattopadhyay, D., Hurley, J., Stevenson, S., & Raidani, A. 2022, arXiv e-prints, arXiv:2202.08924
- Chen, H.-Y., Holz, D. E., Miller, J., Evans, M., Vitale, S., & Creighton, J. 2021, *Classical and Quantum Gravity*, 38, 055010
- Chruslinska, M., & Nelemans, G. 2019, *MNRAS*, 1974
- Conroy, C., & Gunn, J. E. 2010, *ApJ*, 712, 833
- Costa, G., Bressan, A., Mapelli, M., Marigo, P., Iorio, G., & Spera, M. 2021, *MNRAS*, 501, 4514
- de Mink, S. E., & Belczynski, K. 2015, *ApJ*, 814, 58
- de Mink, S. E., & Mandel, I. 2016, *MNRAS*, 460, 3545
- Di Carlo, U. N., et al. 2020, *MNRAS*, 498, 495
- Dominik, M., Belczynski, K., Fryer, C., Holz, D., Berti, B., Bulik, T., Mandel, I., & O'Shaughnessy, R. 2012a, *ApJ*, 759, 52
- Dominik, M., Belczynski, K., Fryer, C., Holz, D. E., Berti, E., Bulik, T., Mandel, I., & O'Shaughnessy, R. 2012b, *ApJ*, 759, 52
- Edelman, B., Doctor, Z., Godfrey, J., & Farr, B. 2022, *ApJ*, 924, 101
- El-Badry, K., Quataert, E., Weisz, D. R., Choksi, N., & Boylan-Kolchin, M. 2019, *Monthly Notices of the Royal Astronomical Society*, 482, 4528
- Farmer, R., Renzo, M., de Mink, S. E., Fishbach, M., & Justham, S. 2020, *ApJ*, 902, L36
- Farrell, E., Groh, J. H., Hirschi, R., Murphy, L., Kaiser, E., Ekström, S., Georgy, C., & Meynet, G. 2021, *MNRAS*, 502, L40
- Fields, C. E., Timmes, F. X., Farmer, R., Petermann, I., Wolf, W. M., & Couch, S. M. 2018, *ApJS*, 234, 19
- Fishbach, M., et al. 2021, *Astrophys. J.*, 912, 98
- Ford, K. E. S., & McKernan, B. 2021, arXiv e-prints, arXiv:2109.03212
- Fragione, G., & Banerjee, S. 2020, *ApJ*, 901, L16
- Fragione, G., Kocsis, B., Rasio, F. A., & Silk, J. 2021, arXiv e-prints, arXiv:2107.04639
- Fryer, C. L., Belczynski, K., Wiktorowicz, G., Dominik, M., Kalogera, V., & Holz, D. E. 2012, *ApJ*, 749, 91
- Fuller, J., & Ma, L. 2019, *ApJ*, 881, L1
- Gaburov, E., Lombardi, J. C., & Portegies Zwart, S. 2008, *MNRAS*, 383, L5
- Gallegos-García, M., Berry, C. P. L., Marchant, P., & Kalogera, V. 2021, *ApJ*, 922, 110
- García, F., Simaz Buzel, A., Chaty, S., Porter, E., & Chassande-Mottin, E. 2021, *A&A*, 649, A114
- Gerosa, D., & Kesden, M. 2016, *PRECESSION: Python toolbox for dynamics of spinning black-hole binaries*, *Astrophysics Source Code Library*, record ascl:1611.004
- Gessner, A., & Janka, H.-T. 2018, *ApJ*, 865, 61
- Giacobbo, N., & Mapelli, M. 2018, *MNRAS*, 480, 2011
- Heggie, D., & Hut, P. 2003, *Classical and Quantum Gravity*, 20, 4504
- Hénon, M. 1971, *Astrophysics and Space Science*, 13, 284
- Hénon, M. H. 1971, *Ap&SS*, 14, 151
- Hobbs, G., Lorimer, D. R., Lyne, A. G., & Kramer, M. 2005, *MNRAS*, 360, 974
- Hurley, J. R., Pols, O. R., & Tout, C. A. 2000, *MNRAS*, 315, 543
- Hurley, J. R., Tout, C. A., & Pols, O. R. 2002, *MNRAS*, 329, 897
- J. C. Lombardi, J., Warren, J. S., Rasio, F. A., Sills, A., & Warren, A. R. 2002, *The Astrophysical Journal*, 568, 939
- Joshi, K. J., Rasio, F. A., & Portegies Zwart, S. P. 2000, *The Astrophysical Journal*, 540, 969
- King, A. R., Davies, M. B., Ward, M. J., Fabbiano, G., & Elvis, M. 2001, *ApJ*, 552, L109
- Kinugawa, T., Nakamura, T., & Nakano, H. 2020, arXiv e-prints, arXiv:2009.06922
- Klencki, J., Moe, M., Gladysz, W., Chruslinska, M., Holz, D. E., & Belczynski, K. 2018, *Astron. Astrophys.*, 619, A77
- Klencki, J., Nelemans, G., Istrate, A. G., & Chruslinska, M. 2021, *A&A*, 645, A54
- Kremer, K., et al. 2020, *ApJ*, 903, 45
- Kroupa, P. 2001, *MNRAS*, 322, 231
- Leung, S.-C., Nomoto, K., & Blinnikov, S. 2019, *ApJ*, 887, 72
- Lipunov, V. M., Postnov, K. A., & Prokhorov, M. E. 1997, *Astronomy Letters*, 23, 492
- MacLeod, M., Antoni, A., Murguía-Berthier, A., Macias, P., & Ramirez-Ruiz, E. 2017, *ApJ*, 838, 56
- Madau, P., & Fragos, T. 2017, *ApJ*, 840, 39
- Mandel, I., & Broekgaarden, F. S. 2021, arXiv e-prints, arXiv:2107.14239
- Mandel, I., & de Mink, S. E. 2016, *MNRAS*, 458, 2634
- Mapelli, M. 2016, *MNRAS*, 459, 3432
- Mapelli, M., et al. 2021, *MNRAS*, 505, 339
- Marchant, P., Langer, N., Podsiadlowski, P., Tauris, T. M., & Moriya, T. J. 2016, *A&A*, 588, A50
- Mikkola, S., & Merritt, D. 2008, *AJ*, 135, 2398
- Mikkola, S., & Tanikawa, K. 1999, *Monthly Notices of the Royal Astronomical Society*, 310, 745
- Moe, M., & Di Stefano, R. 2017, *ApJS*, 230, 15
- Mondal, S., Belczynski, K., Wiktorowicz, G., Lasota, J.-P., & King, A. R. 2020, *MNRAS*, 491, 2747
- Neijssel, C. J., et al. 2019a, *MNRAS*, 490, 3740
- . 2019b, *MNRAS*, 490, 3740
- Nitadori, K., & Aarseth, S. J. 2012, *Monthly Notices of the Royal Astronomical Society*, 424, 545
- O'Connor, E., & Ott, C. D. 2011, *ApJ*, 730, 70
- Olejak, A., & Belczynski, K. 2021, *ApJ*, 921, L2
- Olejak, A., Belczynski, K., & Ivanova, N. 2021, *A&A*, 651, A100
- Olejak, A., Fryer, C. L., Belczynski, K., & Baibhav, V. 2022, arXiv e-prints, arXiv:2204.09061
- Pattabiraman, B., Umbreit, S., Liao, W. K., Choudhary, A., Kalogera, V., Memik, G., & Rasio, F. A. 2013, *The Astrophysical Journal, Supplement Series*, 204, 16
- Pavlovskii, K., Ivanova, N., Belczynski, K., & Van, K. X. 2017, *MNRAS*, 465, 2092
- Peters, P. C. 1964, *Physical Review*, 136, 1224
- Podsiadlowski, P., Langer, N., Poelarends, A. J. T., Rappaport, S., Heger, A., & Pfahl, E. 2004, *ApJ*, 612, 1044
- Podsiadlowski, P., Rappaport, S., & Han, Z. 2003, *MNRAS*, 341, 385
- Portegies Zwart, S. F., & McMillan, S. L. W. 2000, *ApJ*, 528, L17
- Portegies Zwart, S. F., McMillan, S. L. W., & Gieles, M. 2010, *ARA&A*, 48, 431
- Qin, Y., Fragos, T., Meynet, G., Andrews, J., Sørensen, M., & Song, H. F. 2018, *A&A*, 616, A28
- Rastello, S., Amaro-Seoane, P., Arca-Sedda, M., Capuzzo-Dolcetta, R., Fragione, G., & Tosta e Melo, I. 2019, *MNRAS*, 483, 1233
- Rastello, S., Mapelli, M., Di Carlo, U. N., Iorio, G., Ballone, A., Giacobbo, N., Santoliquido, F., & Tornamenti, S. 2021, *MNRAS*, 507, 3612
- Rodriguez, C. L., Amaro-Seoane, P., Chatterjee, S., Kremer, K., Rasio, F. A., Samsing, J., Ye, C. S., & Zevin, M. 2018a, *Phys. Rev. D*, 98, 123005
- Rodriguez, C. L., Amaro-Seoane, P., Chatterjee, S., & Rasio, F. A. 2018b, *Phys. Rev. Lett.*, 120, 151101
- Rodriguez, C. L., Chatterjee, S., & Rasio, F. A. 2016a, *Phys. Rev. D*, 93, 084029
- Rodriguez, C. L., Haster, C.-J., Chatterjee, S., Kalogera, V., & Rasio, F. A. 2016b, *ApJ*, 824, L8
- Rodriguez, C. L., & Loeb, A. 2018, *The Astrophysical Journal Letters*, 866, L5
- Rodriguez, C. L., Zevin, M., Amaro-Seoane, P., Chatterjee, S., Kremer, K., Rasio, F. A., & Ye, C. S. 2019, *Phys. Rev. D*, 100, 043027
- Rodriguez, C. L., Zevin, M., Amaro-Seoane, P., Chatterjee, S., Kremer, K., Rasio, F. A., & Ye, C. S. 2019, *Physical Review D*, 100, 43027
- Roulet, J., Chia, H. S., Olsen, S., Dai, L., Venumadhav, T., Zackay, B., & Zaldarriaga, M. 2021, *Phys. Rev. D*, 104, 083010
- Safarzadeh, M., Hamers, A. S., Loeb, A., & Berger, E. 2020, *ApJ*, 888, L3
- Samsing, J., et al. 2020, arXiv e-prints, arXiv:2010.09765

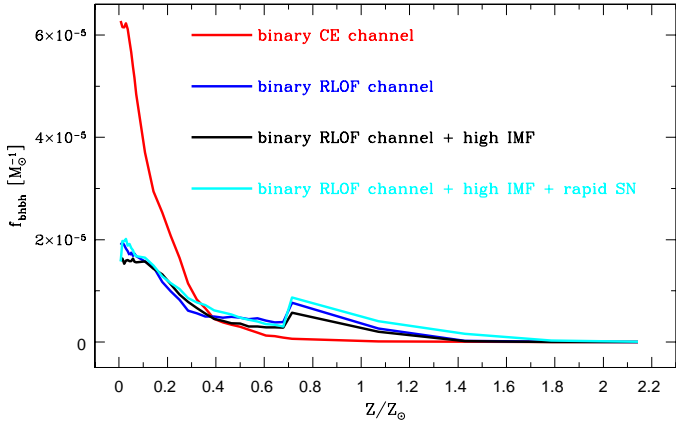


FIG. 3.— BH-BH merger formation efficiency per unit mass as a function of metallicity for the CE and three RLOF isolated binary evolution channels.

Sana, H., & Evans, C. J. 2011, in IAU Symposium, Vol. 272, Active OB Stars: Structure, Evolution, Mass Loss, and Critical Limits, ed. C. Neiner, G. Wade, G. Meynet, & G. Peters, 474–485
 Sana, H., et al. 2012, *Science*, 337, 444
 —. 2013, *A&A*, 550, A107
 Santoliquido, F., Mapelli, M., Giacobbo, N., Bouffanais, Y., & Artale, M. C. 2021, *MNRAS*, 502, 4877
 Schneider, A. S., Roberts, L. F., Ott, C. D., & O’Connor, E. 2019, *Phys. Rev. C*, 100, 055802
 Sharda, P., Krumholz, M. R., Wisnioski, E., Acharyya, A., Federrath, C., & Forbes, J. C. 2021, *MNRAS*, 504, 53
 Spera, M., Mapelli, M., Giacobbo, N., Trani, A. A., Bressan, A., & Costa, G. 2019, *MNRAS*, 485, 889
 Spitzer, L. 1987, *Dynamical evolution of globular clusters*, Princeton University Press, Princeton, NJ, 191 p.
 Stevenson, S., Sampson, M., Powell, J., Vigna-Gómez, A., Neijssel, C. J., Szécsi, D., & Mandel, I. 2019, arXiv e-prints The LIGO Scientific Collaboration et al. 2021a, arXiv e-prints, arXiv:2111.03606
 —. 2021b, *ApJ*, 913, L7

—. 2021c, arXiv e-prints, arXiv:2111.03634
 Timmes, F. X., Woosley, S. E., & Weaver, T. A. 1996, *ApJ*, 457, 834
 Tiwari, V. 2022, *ApJ*, 928, 155
 Tiwari, V., & Fairhurst, S. 2021, *ApJ*, 913, L19
 van den Heuvel, E. P. J., Portegies Zwart, S. F., & de Mink, S. E. 2017, *MNRAS*, 471, 4256
 van Son, L. A. C., et al. 2021, arXiv e-prints, arXiv:2110.01634
 —. 2022, *ApJ*, 931, 17
 Vink, J. S., & de Koter, A. 2005, *A&A*, 442, 587
 Vink, J. S., de Koter, A., & Lamers, H. J. G. L. M. 2001, *A&A*, 369, 574
 Voss, R., & Tauris, T. M. 2003, *MNRAS*, 342, 1169
 Webbink, R. F. 1984, *ApJ*, 277, 355
 Zampieri, L., & Roberts, T. P. 2009, *MNRAS*, 400, 677
 Zevin, M. 2020, *Constraining the Origins of Binary Black Holes using Multiple Formation Pathways*
 Zevin, M., Spera, M., Berry, C. P. L., & Kalogera, V. 2020, *ApJ*, 899, L1
 Zevin, M., et al. 2021, *The Astrophysical Journal*, 910, 152
 Zhang, Q. S. 2013, *ApJS*, 205, 18

5. APPENDIX A

All four binary models show a general increase in the average intrinsic total BH-BH merger mass with redshift (see Fig. 1). However, there is an exception from this trend for the CE BH-BH formation channel at low redshifts ($z \lesssim 2 - 3$). Here, we provide an explanation for this behavior.

For this channel, BH-BH merger formation depends sensitively on radial expansion of BH progenitor stars and thus on metallicity (Belczynski et al. 2010b). For our CE model, we only allow for CEs to develop and successfully form close binaries for late donor evolutionary stages (e.g., during core He-burning). Significant radial expansion during core He-burning is found at low metallicity, as high metallicity H-rich stellar envelopes are usually severely depleted by stellar winds for massive stars. As metallicity of stellar populations increases with decreasing redshift, the CE channel BH-BH merger formation efficiency significantly drops as seen in Figure 3. For low redshifts ($z \lesssim 2 - 3$) the average metallicity of stellar populations becomes significant ($Z > 0.5 Z_{\odot}$, see Fig.7 of Belczynski et al. (2020)) and the formation efficiency of BH-BH mergers is very small. The low mass BH-BH mergers that form from high metallicity stars do not contribute significantly to overall population of BH-BH mergers at these redshifts. The majority of mergers at these redshifts originate from low-metallicity stars that still form in the tail of metallicity distribution even to $z = 0$. Massive mergers that form at low metallicity at high redshifts do not contribute significantly at low redshifts as merger rates fall off steeply with delay time (Dominik et al. 2012a). This sharp drop in BH-BH merger formation efficiency with metallicity (Fig. 3) is responsible for the flat behavior of the average BH-BH merger mass at low redshifts. This does not affect RLOF channels as they depend on expansion of stars at much earlier evolutionary stages (e.g., during the Hertzsprung gap) which are not affected as much by stellar winds and metallicity.

6. APPENDIX B

Here, we explain the difference in average total mass of BH-BH mergers between the CE formation channel and RLOF channels. It is clearly visible that RLOF channels produce much more massive BH-BH mergers at all redshifts (see Fig. 1).

In Figures 5 and 6 we present formation scenarios for typical BH-BH mergers at redshift $z = 6$ in the CE and stable RLOF (standard IMF, delayed SN engine) isolated binary evolution channels, respectively. The two chosen examples of BH-BH systems have their total mass and metallicity close to the average mass $\bar{M}_{\text{tot,int}} = 29.3, 47.7 M_{\odot}$ (CE, RLOF) and the average metallicity $\bar{Z} = 0.0013, 0.0012$ (CE, RLOF) at $z = 6$ for the two channels (see Fig. 4). For

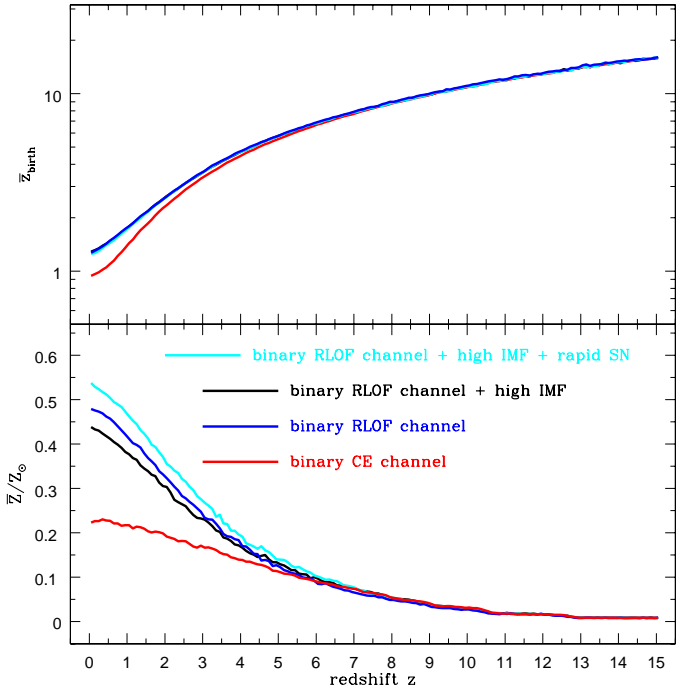


FIG. 4.— Top: average birth redshift of binary progenitors of BH-BH mergers that merge at a given redshift for four isolated binary formation channels. Note that black and cyan lines are right under blue line. Bottom: average metallicity of binaries that produce BH-BH mergers at a given redshift.

the CE channel we show example with $M_{\text{tot,int}} = 31 M_{\odot}$, and for the standard RLOF channel with $M_{\text{tot,int}} = 47 M_{\odot}$. Note the very clear total mass difference of BH-BH mergers from the two formation scenarios. Below we explain the origin of this difference.

The two examples, despite having rather different primary stars ($\sim 38 M_{\odot}$ and $\sim 65 M_{\odot}$ at ZAMS: $t = 0$ Myr), produce the similar mass BHs ($\sim 14 M_{\odot}$) out of the primary stars. This comes from the fact that both primaries are stripped of their H-rich envelopes (first RLOF phase in each case) at different evolutionary stages and their exposed helium cores, Wolf-Rayet (WR) stars, have almost the same mass. In the CE scenario, the first RLOF begins when the primary is on Hertzsprung gap and its helium core is developed after the entirety of main-sequence H-burning. In the RLOF scenario, the first RLOF begins when the primary is still on the main sequence, and due to mass loss the star is de-rejuvenated, producing a much smaller core than would be expected for a single star with the same initial mass. Since both first-formed BHs have the same mass, it means that mass difference between the two BH-BH mergers is directly connected to the secondary star, its mass, and its evolution.

In the CE channel, the secondary mass is $34 M_{\odot}$ at $t = 0$ Myr. It increases to $45 M_{\odot}$ after first stable RLOF event. Then the secondary loses mass in stellar winds to initiate the second RLOF at a mass of $27 M_{\odot}$ when it is core He-burning. This second RLOF is a CE event that leaves the secondary as a naked helium core (WR star) with a mass of $17 M_{\odot}$, which quickly collapses to a BH with similar mass. Note the significant orbital separation decay during the CE phase, from $a = 482 R_{\odot}$ to $a = 9.5 R_{\odot}$. If we made the binary at this stage instead proceed through stable RLOF, then there would be not enough orbital contraction to produce a merging BH-BH system. Simply, the secondary star would not have enough mass in its envelope to allow for enough associated angular momentum loss from the binary to provide significant orbital decay. The orbital decay would be rather small: from $a = 482 R_{\odot}$ to $a = 440 R_{\odot}$, producing a BH-BH system with an inspiral time much larger than the Hubble time.

In the RLOF channel, the secondary starts with a mass of $64 M_{\odot}$. It increases to $87 M_{\odot}$ after the first stable RLOF event. Then the secondary, with almost no mass loss: $85 M_{\odot}$ (mostly main-sequence evolution with a relatively small stellar radius), initiates the second RLOF event right after the main sequence when it is on the Hertzsprung gap. The second RLOF is stable thermal-timescale mass transfer. The RLOF strips the secondary of its envelope, leaving a WR star with a mass of $38 M_{\odot}$. After losing about $5 M_{\odot}$ to winds, the WR star collapses to a massive BH of $33 M_{\odot}$. This second RLOF event reduces orbital separation from $a = 295 R_{\odot}$ to $a = 6.2 R_{\odot}$, producing a close BH-BH system that can merge in the Hubble time. The high mass of the donor star (secondary) in this event is required to allow for significant decay of the orbit. During thermal-timescale mass transfer, almost the entirety of the donor's envelope is lost from the binary (highly over-Eddington mass transfer rate), taking away binary angular momentum and reducing the size of the orbit (as long as donor mass is larger than accretor mass). In order to form a BH-BH binary system close enough to merge in the Hubble time through two stable RLOF episodes, the donor star needs to be few times more massive than its BH companion at the onset of the second RLOF event (van den Heuvel et al. 2017; Olejak et al. 2021). Only such unequal mass binaries ($q_{\text{RLOF}} = \frac{M_{\text{don}}}{M_{\text{acc}}} \gtrsim 3$) are able to eject a large enough amount of mass and orbital angular momentum to reduce the orbital separation enough to produce merging BH-BH systems.

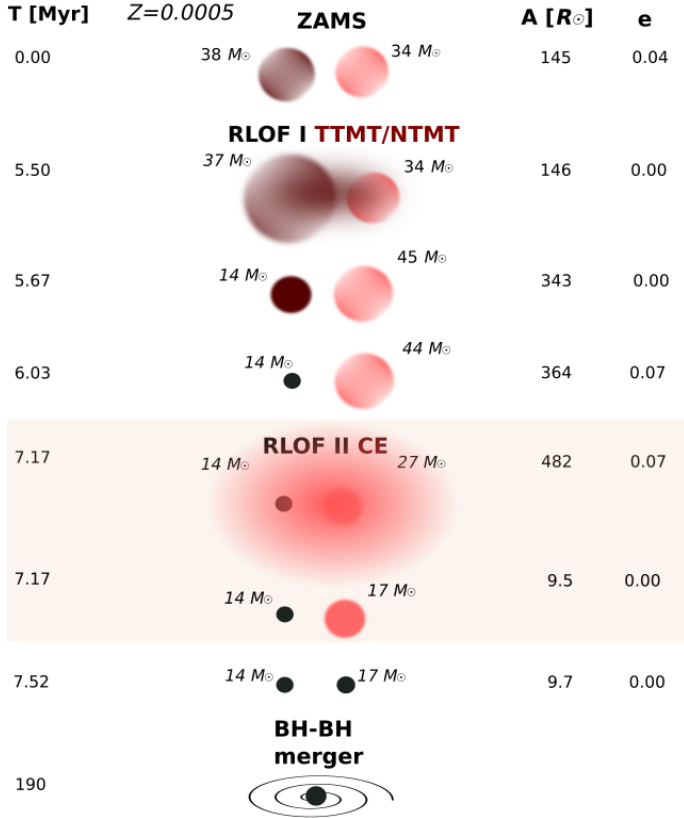


FIG. 5.— The formation scenario for a typical BH-BH merger at redshift $z \approx 6$ in the classical (CE) isolated binary evolution channel. The shaded part of the evolution shows the most important part of evolution that leads to orbital decay, allowing for the formation of close BH-BH binary that can merge in the Hubble time.

If at onset of the second RLOF event we applied CE evolution instead of stable mass transfer, then the ejection of very massive envelope of the secondary ($47 M_{\odot}$) would lead to post-CE separation of only $a = 0.7 R_{\odot}$. This is smaller than the radius of a secondary core (a WR star: $> 1 - 2 R_{\odot}$; Hurley et al. (2000)) and thus CE evolution would lead to a merger of the BH with the massive secondary and no formation of a BH-BH system. Note that in our standard simulations we would not even attempt to perform CE evolution for such a case, as the donor (secondary) is on Hertzsprung gap at the onset of RLOF and has a radiative envelope that would not allow for the development/survival of a CE (Belczynski et al. 2007; Klencki et al. 2021).

Of course, to alleviate this issue one may require the formation of a much wider binary at the onset of the second RLOF event in this case. Then, not only may there be enough orbital energy to successfully expel the CE, but also the donor star would be core He-burning and much more extended, as well as having a convective envelope. However, such star has already evolved through most its life and lost a significant fraction of its H-rich envelope through stellar winds. In such a case, even very efficient CE evolution may not be enough to decay the orbit below the threshold of formation of merging BH-BH systems. It is possible, but it requires fine tuning, and for a given model of CE efficiency and adopted stellar winds only few systems form massive BH-BH mergers in the CE channel. This was already proposed and explained, although in somewhat different terms, by van Son et al. (2021), and our detailed description is provided only to serve as a replication study.

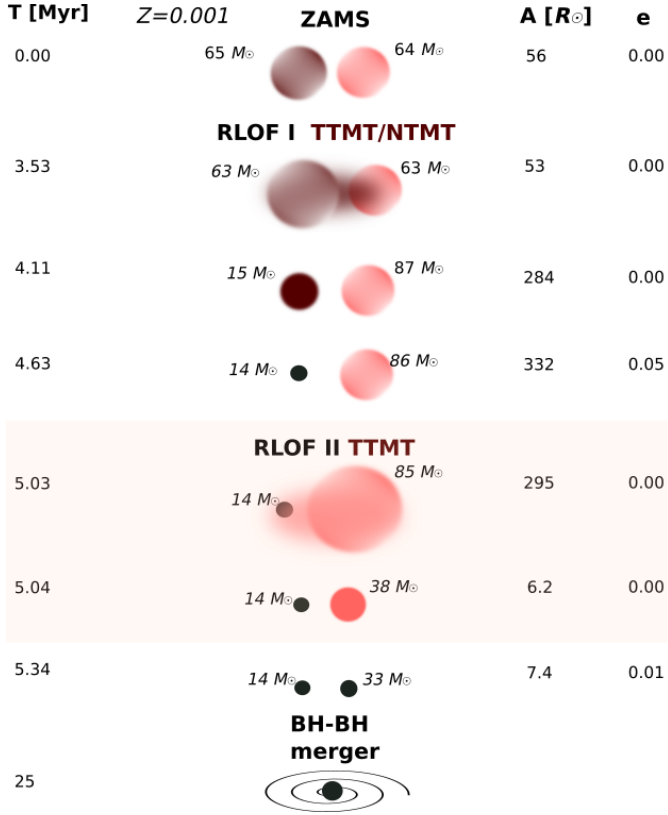


FIG. 6.— The formation scenario for a typical BH-BH merger at redshift $z \approx 6$ in the stable RLOF channel (standard IMF, delayed SN engine). The shaded part of the evolution shows the most important part of evolution that leads to orbital decay, allowing for the formation of close BH-BH binary that can merge in the Hubble time.